



Peculiar Prompt Emission and Afterglow in the H.E.S.S.-detected GRB 190829A

Vikas Chand^{1,2}, Ankush Banerjee¹¹, Rahul Gupta^{3,4}, Dimple^{3,4}, Partha Sarathi Pal⁵, Jagdish C. Joshi^{1,2}, Bin-Bin Zhang^{1,2,6}, R. Basak^{7,8}, P. H. T. Tam⁵, Vidushi Sharma⁹, S. B. Pandey³, Amit Kumar^{3,10}, and Yi-Si Yang^{1,2}

¹ School of Astronomy and Space Science, Nanjing University, Nanjing 210093, People's Republic of China; vikasK2@nju.edu.cn, bbzhang@nju.edu.cn

² Key Laboratory of Modern Astronomy and Astrophysics (Nanjing University), Ministry of Education, People's Republic of China

³ Aryabhata Research Institute of Observational Sciences (ARIES), Manora Peak, Nainital-263002, India

⁴ Department of Physics, Deen Dayal Upadhyaya Gorakhpur University, Gorakhpur 273009, India

⁵ School of Physics and Astronomy, Sun Yat Sen University, Guangzhou 510275, People's Republic of China

⁶ Department of Physics and Astronomy, University of Nevada, Las Vegas, NV 89154, USA

⁷ INFN-OAS Bologna, Via P. Gobetti 101, I-41129 Bologna, Italy

⁸ Department of Physics and Earth Sciences, University of Ferrara, Block C, Via Saragat-1, I-41122 Ferrara, Italy

⁹ Inter University Centre for Astronomy and Astrophysics, Pune, India

¹⁰ School of Studies in Physics and Astrophysics, Pandit Ravishankar Shukla University, Chattisgarh 492 010, India

Received 2020 January 2; revised 2020 May 20; accepted 2020 May 21; published 2020 July 21

Abstract

We present the results of a detailed investigation of the prompt and afterglow emission in the High Energy Stereoscopic System (H.E.S.S.)-detected GRB 190829A. Swift and Fermi observations of the prompt phase of this gamma-ray burst (GRB) reveal two isolated subbursts or episodes, separated by a quiescent phase. The energetic and the spectral properties of the first episode are in stark contrast to the second. The first episode, which has a higher spectral peak ~ 120 keV and a low isotropic energy $\sim 10^{50}$ erg is an outlier to the Amati correlation and marginally satisfies the Yonetoku correlation. However, the energetically dominant second episode has lower peak energy and is consistent with the above correlations. We compared this GRB to other low-luminosity GRBs (LLGRBs). Prompt emission of LLGRBs also indicates a relativistic shock breakout origin of the radiation. For GRB 190829A, some of the properties of a shock breakout origin are satisfied. However, the absence of an accompanying thermal component and energy above the shock breakout critical limit precludes a shock breakout origin. In the afterglow, an unusual long-lasting late-time flare of duration $\sim 10^4$ s is observed. We also analyzed the late-time Fermi Large Area Telescope (LAT) emission that encapsulates the H.E.S.S. detection. Some of the LAT photons are likely to be associated with the source. All of the above observational facts suggest GRB 190829A is a peculiar low-luminosity GRB that is not powered by a shock breakout, and has an unusual rebrightening due to patchy emission or a refreshed shock during the afterglow. Furthermore, our results show that teraelectronvolt-energy photons seem common in both high-luminosity GRBs and LLGRBs.

Unified Astronomy Thesaurus concepts: Gamma-ray bursts (629); Burst astrophysics (187); High energy astrophysics (739)

1. Introduction

Radiation mechanisms in the prompt emission of gamma-ray bursts (GRBs) remain a highly debated topic. The afterglow phase, in general, is well explained by the emission originating from external shocks produced by a blast wave inevitably crashing into the circumburst medium, and any deviations from this model can also be addressed (e.g., see Kumar & Zhang 2015; Mészáros 2019 for a review).

The recent detections of GRB afterglow in teraelectronvolt energies¹² by the High Energy Stereoscopic System (H.E.S.S.) and Major Atmospheric Gamma Imaging Cerenkov (MAGIC) telescopes have provided new insights into the study of GRBs (Abdalla et al. 2019; de Naurois 2019; MAGIC Collaboration et al. 2019a). For example, GRB 190114C, in its multi-frequency spectral energy density, showed evidence for a double-peaked distribution with the first peak being the synchrotron emission. The second peak shows a very high energy (VHE) emission in teraelectronvolt energies and is explained by the synchrotron self-Comptonisation process, theoretically predicted in a standard afterglow model (MAGIC Collaboration et al. 2019b). GRB 180720B also showed a VHE

emission at late times that could be explained by the inverse-Compton mechanism (Abdalla et al. 2019).

While afterglow studies have progressed considerably, the prompt emission is still challenging to understand. A lot of empirical models have been proposed, which include the traditional Band function (Band et al. 1993) and deviations from this simple shape modeled by adding an extra thermal component, breaks, or multiple spectral components (Ryde 2005; Abdo et al. 2009; Guiriec et al. 2011, 2015a, 2015b; Page et al. 2011; Ackermann et al. 2013; Basak & Rao 2015; Guiriec et al. 2016; Vianello et al. 2017; Ravasio et al. 2018). The recent developments in the physical modeling of the prompt emission show that the synchrotron could be the main emission mechanism (Oganesyan et al. 2019; Burgess et al. 2020). However, the physical photospheric models also explain the data equally well (Vianello et al. 2017; Ahlgren et al. 2019; Acuner et al. 2020). In this context, it is important to study the prompt emission properties of the GRBs detected by the H.E.S.S. and MAGIC telescopes to get a global picture and capture the diversity of these events.

Studies on GRB 190114C showed multiple components in its prompt emission and a standard afterglow (Chand et al. 2019; Fraija et al. 2019a; Ravasio et al. 2019b; Wang et al. 2019). GRB 180720B has synchrotron spectrum for prompt emission

¹¹ Private Astronomer.

¹² Several hundred gigaelectronvolts.

and a standard afterglow (Fraija et al. 2019b; Ronchi et al. 2019). GRB 190829A is another such GRB detected by H.E.S.S. at a redshift of 0.0785 (de Naurois 2019; Valeev et al. 2019). Compared to the previously detected VHE events, it has a lower luminosity. Prompt emission of LLGRBs also indicates a relativistic shock breakout origin of the radiation (Nakar & Sari 2012). Here we report the spectral and temporal analysis of the Neil Gehrels Swift Observatory and Fermi Gamma-ray Space Telescope data and multiwavelength observations of this event.

2. Prompt Observations and Analysis

GRB 190829A triggered the Fermi/Gamma-ray Burst Monitor (GBM) at 2019 August 29 19:55:53.13 UTC (T_0 ; Lesage et al. 2019) and the Swift/Burst Alert Telescope (BAT) at 19:56:44.60 UTC (Lien et al. 2019). The Swift/X-ray Telescope (XRT) observed the GRB from 97.3 s after the BAT trigger time and refined the location to R.A. (J2000): $02^{\text{h}} 58^{\text{m}} 10^{\text{s}}.57$ and decl. (J2000): $-08^{\circ} 57' 28''.6$ (Dichiara et al. 2019). H.E.S.S. detected a teraelectronvolt signal 4.2 hrs after the prompt emission in a direction consistent with this location. In a multiwavelength observation campaign, GRB 190829A was followed by several optical, near-IR (NIR), and radio telescopes (Section 3).

During the prompt emission, both Fermi and Swift detected two episodes, the first episode starting from T_0 to $T_0 + 4$ s followed by a brighter episode from $T_0 + 47.1$ s to $T_0 + 61.4$ s. The spectrum of the first episode in the Fermi data is best described by a power law with an exponential high-energy cutoff function having an index of -1.41 ± 0.08 , and a cutoff energy corresponding to a peak energy, $E_p = 130 \pm 20$ keV (Lesage et al. 2019). The second episode is best fitted by a Band function (Band et al. 1993) with $E_p = 11 \pm 1$ keV, $\alpha = -0.92 \pm 0.62$, and $\beta = -2.51 \pm 0.01$. The observed fluence is $1.27 \pm 0.02 \times 10^{-5}$ erg cm $^{-2}$ in the 10–1000 keV band with the episodes combined (Lesage et al. 2019). From the preliminary spectral results, reported in Fermi GBM Team (2019), we note the different nature of the two episodes.

In our analysis of Fermi-GBM data, we identified NaI detector numbers 6 and 7 (n6 and n7) by visually examining count rates and with observing angles $< 50^\circ$ to the source position. The angle constraints are to avoid the systematics arising due to uncertainty in the response at larger angles. Among the bismuth germanate (BGO) detectors, BGO 1 (b1) is selected as it is closer to the direction of the GRB. The time-tagged event data was reduced using Fermi Science Tools software `gtburst`.¹³ We used XSPEC (Arnaud 1996) to model the spectrum. The Bayesian information criteria (BIC) is calculated for each model from the `pgstat` value (Kass & Raftery 1995). In all these models used, the power-law model has the least BIC. The Swift-BAT spectrum is obtained in the BAT mission elapsed times corresponding to the times of our selection for joint spectral analysis. The recipe followed for reducing the spectrum is as described in the Swift-BAT software guide.¹⁴ We use HEASOFT software v6.25 with the latest calibration database.¹⁵ We applied gain correction using `bateconvert`, then `batbinevt` was utilized to produce a spectrum after making a detector plane image, retrieving problematic

Table 1
Properties of Two Episodes in GRB 190829A

Properties	Episode 1	Episode 2
T_{90} (s) in 50–300 keV	6.30 ± 0.08	10.37 ± 0.05
t_q (s)	~ 40	
HR	0.57	0.15
E_p (keV)	$120.0^{+111.7}_{-37.2}$	$10.9^{+0.5}_{-0.6}$
F (10^{-6} erg cm $^{-2}$)	$2.4^{+0.7}_{-0.4}$	$13.8^{+0.4}_{-0.4}$
$E_{\gamma, \text{iso}}$ (erg)	3.2×10^{49}	1.9×10^{50}
$L_{p, \text{iso}}$ (erg s $^{-1}$)	8.6×10^{48}	2.9×10^{49}
Redshift z	0.0785 ± 0.005	
Energy band (keV)	Lag (correlation) ms (%)	
8–30	71 ± 3 (63)	100 ± 4 (65)
8–100	81 ± 2 (66)	40 ± 3 (66)

Note. Spectral lags are measured at 8 ms bin and w.r.t. 150–300 keV. T_{90} : duration from GBM data; t_q : quiescent time; hardness ratio (HR): ratio of the counts in 50–300 keV to the counts in 10–50 keV; E_p : time-integrated peak energy calculated using joint BAT (15–150 keV) and GBM (8 keV–40 MeV) data; F : energy fluence; $E_{\gamma, \text{iso}}$: isotropic energy; $L_{p, \text{iso}}$: isotropic peak luminosity.

detectors, removing hot pixels, and subtracting the background using `batbinevt`, `batdetmask`, `bathotpix`, and `batmaskwtevt`, respectively. Additionally, FTOOLS `batupdatephakw` and `batphasyserr` are used for compensating the observed residual in the responses and for making sure that we have the position of the burst in instrument coordinates. We have generated the detector response matrix using `batdrmggen`. For a joint analysis of BAT–GBM data (see Figures 2 and A1 and Table 1), the GBM data are grouped to result in minimum 20 counts and χ^2 statistics are optimized for finding the best-fit parameters. All quoted errors on spectral parameters correspond to 1σ (nominal 68%).

2.1. The Peculiar Nature of the Episodes

2.1.1. Light Curve and Spectrum

In Figure 1, we have shown the light curves of the prompt emission phase in a wide energy band: 8–900 keV of GBM–NaI, 0.3–1 MeV of GBM–BGO. The GRB appears to have a softer spectrum, as can be inferred from the low signal of the BGO light curve. To examine this further, we plotted the hardness ratio (H/S) in two bands of the NaI light curve, where the harder band is 50–300 keV, and the softer band is 8–50 keV. We note that the first episode has comparable count rates in these two energy bands, while the second episode has a much higher rate in the softer band, implying a relatively softer nature of this episode. This is also reflected in the time-integrated spectrum of the individual episodes. Spectral analysis shows that the first episode can be modeled by a power-law (index α) with an exponential cutoff, where the cutoff energy (E_c) can be reparameterized in terms of peak energy $E_p = (2+\alpha) E_c$. The second episode, when modeled with a simple power law, has a steeper spectral index. The properties calculated from spectral parameters for the two episodes are reported in Table 1.

¹³ <https://fermi.gsfc.nasa.gov/ssc/data/analysis/scitools/gtburst.html>

¹⁴ http://swift.gsfc.nasa.gov/analysis/bat_swguide_v6_3.pdf

¹⁵ <https://heasarc.gsfc.nasa.gov/FTP/caldb/>

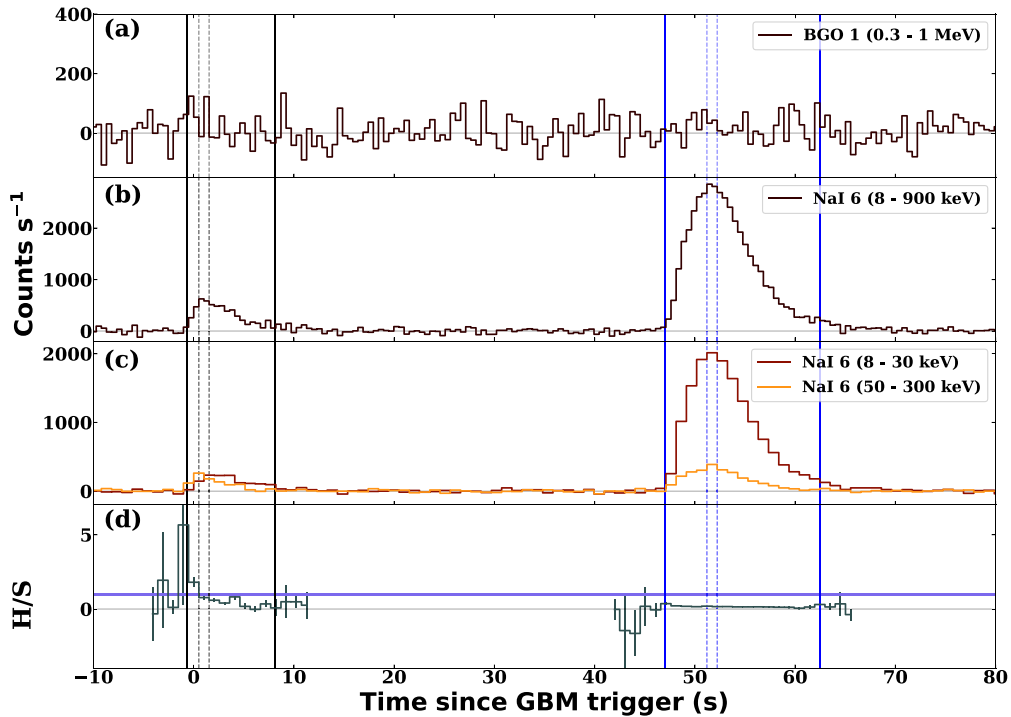


Figure 1. Multichannel light curves: the background-subtracted count rate of GRB 190829A with time in multiple energy bands (a)–(c). (d) The hardness ratio (H/S) in energy bands 50–300 keV (H) and 8–30 keV (S) is shown. The horizontal violet line indicates equal rates in H and S bands. The vertical black and blue lines indicate the boundaries of T_{90} (solid lines) and peak luminosity (dashed lines) calculations for the first and second emission episodes, respectively.

We resolved the 8–900 keV light curve into smaller bins based on the signal-to-noise ratio (S/N) to study the spectral evolution. We created a total of 21 spectra: 5 (S/N = 15) and 16 (S/N = 30) for the first and the second episodes, respectively. The cutoff in the power-law model (COMP) is also preferred in the time-resolved analysis of the first episode based on the BIC values, see Table 2. We also see that the spectrum softens with time. The spectral index is $< -2/3$ (within the synchrotron slow cooling limit), and therefore the emission of the first episode can have a synchrotron origin. The spectra of the second episode are best fitted by a power-law function with indices < -2 . The index is plausibly related to the higher energy power-law of the Band function. When modeled with the Band function, the peak energies are found to be near the lower edge of the Fermi spectral window (i.e., ~ 8 keV), and hence are probably unphysical as only a few channels are available for the determination of α , e.g., in the case of GRB 171010A (Ravasio et al. 2019a). This is also reflected in erratically changing α , which remained unconstrained throughout, see Table 2.

2.1.2. Amati and Yonetoku Correlations

The spectral peak energy of GRBs in the cosmological rest frame ($E_{p,z}$) is correlated to the isotropic equivalent energy ($E_{\gamma,iso}$) and isotropic peak luminosity ($L_{\gamma,iso}$) in the γ -ray band, see Amati (2006), Yonetoku et al. (2004). Amati correlation is also valid for pulse-wise sample of GRBs (Basak & Rao 2013). GRB 980425B, GRB 031203A, and GRB 171205A do not satisfy the Amati correlation. GRB 061021 is a notable outlier to both the correlations (Nava et al. 2012). These correlations have been used to classify individual episodes in GRBs with long quiescent phases (Zhang et al. 2018). We consider these correlations for GRB 190829A, in its two episodes of activity.

To check whether the Amati correlation is also followed by individual episodes of two-episode GRBs with a quiescent phase, we chose the sample of 101 GRBs from Lan et al. (2018). Among these, there are 11 GRBs with a known redshift are plotted in Figures 2(a) and (b). For the rest, the redshift is varied from 0.1 to 10 and their tracks in the correlation plane are studied. Interestingly, all the individual episodes fall within 3σ intrinsic dispersion of the corresponding correlations (see Figure A1 for the tracks and Table A1 for the spectral parameters). But, the first hard episode of GRB 190829A is an outlier to the Amati correlation and marginally satisfies the Yonetoku correlation.

2.1.3. HR versus T_{90} , Spectral Lag

Short GRBs do not follow the same trend in the Amati correlation as the long GRBs. Here we investigate the intriguing possibility that the two episodes of GRB 190829A show the properties of the two classes of GRBs. In Figure 2(c), we show the position of the two episodes in the Amati correlation plane of the short and long GRB populations (Zhang et al. 2018). Interestingly, the first episode lies with the short GRB population. Classification of long and short GRBs is conventionally studied using their distribution in the hardness-duration plane. The duration, T_{90} , is calculated by the time period when 5% to 95% of the total photon fluence is accumulated. We obtained the episode-wise time-integrated HR by dividing the counts in 10–50 keV and 50–300 keV energy bands to make a comparison with other Fermi GRBs also used in Goldstein et al. (2017). The errors in T_{90} and HR are calculated by simulating 10,000 light curves by adding a Poissonian noise with the mean values at observed errors (Minaev et al. 2014; Narayana Bhat et al. 2016). The T_{90} and HR values for GRB 190829A are presented in Table 1. In

Table 2
Time-resolved Spectral Fitting of Prompt Emission Episodes 1 and 2 (Fermi-GBM) and Spectral Fitting of the Afterglow Phases

Prompt Emission Episode 1												
Time (s)	PL		COMP			Band						
	α	pgstat(BIC) dof = 467	α	E_p (keV)	pgstat(BIC) dof = 466	α	β	E_p (keV)	pgstat(BIC) dof = 465			
−0.64–0.85	$1.49^{+0.06}_{-0.05}$	463.6(494.4)	$1.14^{+0.19}_{-0.21}$	311^{+324}_{-112}	453.5(490.5)	$-1.01^{+0.36}_{-0.28}$	$-1.89^{+0.26}_{-1.89}$	194^{+314}_{-84}	452.3(495.4)			
0.85–1.64	$1.63^{+0.08}_{-0.07}$	490.8(521.6)	$1.26^{+0.27}_{-0.31}$	155^{+279}_{-52}	484.2(521.1)	$-0.75^{+0.75}_{-0.64}$	$-1.88^{+0.19}_{-0.95}$	65^{+132}_{-35}	480.8(523.9)			
1.64–2.72	$1.78^{+0.08}_{-0.08}$	532.9(563.7)	$1.22^{+0.28}_{-0.33}$	86^{+42}_{-19}	517.1(554.0)	$-1.07^{+0.72}_{-0.32}$	$-2.46^{+0.45}_{-2.46}$	71^{+38}_{-30}	516.3(559.4)			
2.72–3.96	$1.87^{+0.10}_{-0.09}$	480.0(510.8)	$1.43^{+0.34}_{-0.40}$	68^{+66}_{-18}	474.6(511.6)	$-1.20^{+0.66}_{-0.46}$	$-2.30^{+0.32}_{-2.30}$	52^{+41}_{-17}	472.8(515.9)			
3.96–8.06	$2.18^{+0.14}_{-0.12}$	540.8(571.6)	$1.83^{+0.05}_{-0.45}$	21^{+18}_{-16}	537.2(574.2)	$-0.43^{+0.43}_{-1.99}$	$-2.34^{+0.20}_{-2.34}$	19^{+18}_{-6}	536.5(579.6)			
Prompt Emission Episode 2												
Time (s)	PL		CPL		Band					BB+PL		
	α	pgstat(BIC) dof = 450	α	E_c (keV)	pgstat(BIC) dof = 449	α	β	E_p (keV)	pgstat(BIC) dof = 448	α	kT (keV)	pgstat(BIC) dof = 448
47.04–49.03	$2.31^{+0.06}_{-0.06}$	452.4(483.0)	$2.12^{+0.14}_{-0.15}$	240^{+605}_{-115}	446.1(482.8)	$0.75^{+0.05}_{-0.95}$	$-2.38^{+0.05}_{-0.06}$	$14.02^{+1.44}_{-0.18}$	442.6(485.5)	$2.20^{+0.11}_{-0.12}$	$4.2^{+1.7}_{-0.8}$	446.9(489.7)
49.03–49.68	$2.48^{+0.06}_{-0.06}$	471.3(501.9)	$2.27^{+0.18}_{-0.17}$	182^{+745}_{-85}	466.3(503.0)	$-1.00^{+1.00}_{-1.12}$	$-2.57^{+0.08}_{-0.25}$	$12.29^{+2.18}_{-5.17}$	462.0(504.8)	$2.43^{+0.12}_{-0.12}$	$5.0^{+4.2}_{-1.3}$	464.6(507.4)
49.68–50.21	$2.43^{+0.06}_{-0.06}$	573.2(603.8)	$2.41^{+0.07}_{-0.13}$	$2278^{+0.00}_{-1967}$	573.1(609.8)	$0.98^{+0.00}_{-0.98}$	$-2.44^{+0.06}_{-0.06}$	$10.49^{+1.74}_{-0.11}$	571.5(614.4)	$2.39^{+0.15}_{-0.13}$	$4.4^{+5.6}_{-4.4}$	572.0(614.9)
50.21–50.66	$2.46^{+0.06}_{-0.05}$	400.1(430.6)	$2.33^{+0.14}_{-0.16}$	328^{+6799}_{-185}	397.0(433.6)	$1.00^{+0.00}_{-1.00}$	$-2.51^{+0.07}_{-0.07}$	$11.94^{+1.42}_{-0.17}$	392.4(435.3)	$2.38^{+0.15}_{-0.12}$	$3.4^{+0.00}_{-2.4}$	398.0(440.8)
50.66–51.11	$2.50^{+0.06}_{-0.06}$	501.3(531.9)	$2.50^{+0.04}_{-0.08}$...	501.3(538.1)	$0.96^{+0.00}_{-0.96}$	$-2.51^{+0.04}_{-0.04}$	$9.44^{+1.99}_{-0.10}$	501.0(543.6)	$2.34^{+0.14}_{-0.14}$	$2.9^{+0.6}_{-0.8}$	497.0(539.5)
51.11–51.52	$2.40^{+0.06}_{-0.05}$	488.0(518.2)	$2.26^{+0.14}_{-0.16}$	299^{+3034}_{-164}	484.0(520.8)	$-1.36^{+1.36}_{-0.50}$	$-2.52^{+0.09}_{-0.11}$	$13.41^{+3.06}_{-8.05}$	475.2(518.0)	$2.30^{+0.10}_{-0.12}$	$4.8^{+1.6}_{-0.8}$	475.0(517.9)
51.52–51.93	$2.44^{+0.06}_{-0.05}$	497.8(528.4)	$2.40^{+0.09}_{-0.13}$	$1324^{+0.00}_{-1048}$	497.4(534.1)	$-1.81^{+1.81}_{-0.65}$	$-2.49^{+0.08}_{-0.10}$	$5.92^{+7.44}_{-2.46}$	495.0(537.8)	$2.34^{+0.11}_{-0.13}$	$4.1^{+1.7}_{-0.8}$	493.0(535.8)
51.93–52.37	$2.44^{+0.05}_{-0.06}$	515.1(545.7)	$2.44^{+0.04}_{-0.10}$...	515.1(551.8)	$0.98^{+0.00}_{-0.80}$	$-2.48^{+0.07}_{-0.07}$	$12.07^{+1.48}_{-0.13}$	508.4(551.2)	$2.22^{+0.13}_{-0.15}$	$3.7^{+0.5}_{-0.4}$	503.0(545.8)
52.37–52.80	$2.47^{+0.06}_{-0.06}$	431.6(462.2)	$2.34^{+0.14}_{-0.16}$	315^{+5454}_{-174}	428.5(465.3)	$0.91^{+0.00}_{-1.49}$	$-2.52^{+0.05}_{-0.05}$	$12.05^{+1.50}_{-0.13}$	425.9(468.7)	$2.40^{+0.06}_{-0.13}$	$4.1^{+3.9}_{-1.0}$	428.3(471.1)
52.80–53.26	$2.46^{+0.06}_{-0.06}$	501.8(532.4)	$2.36^{+0.14}_{-0.15}$	$393^{+0.00}_{-237}$	500.0(536.7)	$1.00^{+0.00}_{-10.95}$	$-2.52^{+0.07}_{-0.08}$	$12.37^{+1.49}_{-0.14}$	494.8(537.7)	$2.32^{+0.13}_{-0.13}$	$3.6^{+1.0}_{-0.6}$	496.4(539.2)
53.26–53.77	$2.47^{+0.06}_{-0.05}$	453.8(484.4)	$2.39^{+0.11}_{-0.13}$	$568^{+0.00}_{-366}$	452.1(488.8)	$-2.05^{+2.05}_{-0.07}$	$-2.50^{+0.07}_{-0.08}$	$10.39^{+2.33}_{-0.12}$	454.0(496.6)	$2.42^{+0.17}_{-0.12}$	$4.0^{+0.00}_{-4.0}$	452.6(495.5)
53.77–54.39	$2.53^{+0.06}_{-0.06}$	481.2(511.8)	$2.47^{+0.11}_{-0.16}$	$682^{+0.00}_{-503}$	481.0(517.5)	$-1.63^{+1.63}_{-0.87}$	$-2.63^{+0.09}_{-0.11}$	$8.16^{+5.40}_{-5.08}$	474.0(516.8)	$2.38^{+0.13}_{-0.15}$	$4.0^{+1.0}_{-0.5}$	470.6(513.4)
54.39–55.08	$2.56^{+0.07}_{-0.06}$	419.0(448.7)	$2.52^{+0.11}_{-0.19}$	$739^{+0.00}_{-592}$	417.7(454.4)	$-1.13^{+1.13}_{-2.15}$	$-2.64^{+0.09}_{-0.15}$	$10.00^{+2.96}_{-4.19}$	413.7(456.5)	$2.47^{+0.13}_{-0.17}$	$4.0^{+1.9}_{-0.7}$	412.3(455.2)
55.08–56.02	$2.55^{+0.06}_{-0.07}$	517.2(547.8)	$2.53^{+0.06}_{-0.17}$	$3607^{+0.00}_{-3402}$	517.2(553.9)	$0.99^{+0.00}_{-0.79}$	$-2.60^{+0.08}_{-0.09}$	$11.53^{+1.38}_{-0.12}$	511.4(554.3)	$2.41^{+0.14}_{-0.17}$	$3.5^{+1.4}_{-0.6}$	513.0(554.9)
56.02–57.50	$2.55^{+0.07}_{-0.07}$	498.3(528.9)	$2.55^{+0.07}_{-0.12}$...	498.3(535.0)	$-0.40^{+0.40}_{-3.13}$	$-2.61^{+0.08}_{-0.10}$	$10.71^{+1.85}_{-2.81}$	494.4(537.2)	$2.29^{+0.17}_{-0.17}$	$3.3^{+0.4}_{-0.4}$	487.4(530.2)
57.50–62.46	$2.64^{+0.09}_{-0.08}$	507.1(537.7)	$2.64^{+0.08}_{-0.10}$...	507.1(543.8)	$0.95^{+0.00}_{-3.44}$	$-2.70^{+0.07}_{-0.08}$	$10.44^{+1.45}_{-0.12}$	504.0(546.8)	$2.16^{+0.21}_{-0.21}$	$2.9^{+0.2}_{-0.3}$	488.3(531.1)
Afterglow												
(Phase) Time (s)	Detectors	Tbabs*zTbabs*cflux*PL										
		n_H	α	Statistics(BIC)								
(I) 104–228	XRT +BAT	$0.84^{+0.27}_{-0.20}$	$2.11^{+0.20}_{-0.17}$	125.1/103								
(IV-prebreak) 23.7 k–167 k	XRT	$1.03^{+0.13}_{-0.12}$	$2.02^{+0.12}_{-0.11}$	532.1/541								
(IV postbreak) 167 k–1550 k	XRT	$1.12^{+0.13}_{-0.12}$	$2.35^{+0.13}_{-0.13}$	486.76/489								
(Phase) Time (s)	Detectors	redden*phabs*zdust*PL				redden*phabs*zdust*bknpower						
		n_H	Γ	Statistics(BIC)	E_{B-V}	n_H	Γ_1	Γ_2	E_b	Statistics(BIC)	E_{B-V}	
(III-pre) 147–620	UVOT + XRT	$0.86^{+0.23}_{-0.20}$	$1.84^{+0.14}_{-0.15}$	39.7/26	$1.14^{+0.25}_{-0.28}$	$0.80^{+0.32}_{-0.38}$	$1.50^{+0.29}_{-0.54}$	$3.14^{+0.85}_{-0.44}$	$3.54^{+3.54}_{-0.89}$	25.9/24	$0.67^{+0.43}_{-0.63}$	
(III-rise) 620-1120	UVOT + XRT	$1.26^{+0.33}_{-0.23}$	$1.92^{+0.21}_{-0.12}$	56.5/30	$1.08^{+0.48}_{-0.25}$	

Table 2
(Continued)

(Phase) Time (s)	Detectors	reden*phabs*zdust*PL				reden*phabs*zdust*bknpower					
		n_H	Γ	Statistics(BIC)	E_{B-V}	n_H	Γ_1	Γ_2	E_b	Statistics(BIC)	E_{B-V}
(III-top) 1120-1700	UVOT + XRT	$1.41^{+0.07}_{-0.07}$	$1.99^{+0.05}_{-0.04}$	404.3/353	$1.33^{+0.11}_{-0.10}$	$1.36^{+0.07}_{-0.07}$	$1.84^{+0.07}_{-0.06}$	$2.59^{+0.81}_{-0.55}$	$2.15^{+0.17}_{-0.09}$	378.9/351	$1.04^{+0.14}_{-0.12}$

Note. a : $\chi^2/\text{degrees of freedom (dof)}$ for joint BAT-XRT data and UVOT-XRT data and C-stat for XRT data. All errors are quoted at 1σ (nominal 68%) confidence level. $N_H(z)$: in units of 10^{22} cm^{-2} ; E_b are the break and cutoff energies, respectively, in units of keV. Reddening parameter in host is obtained for SMC extinction law.

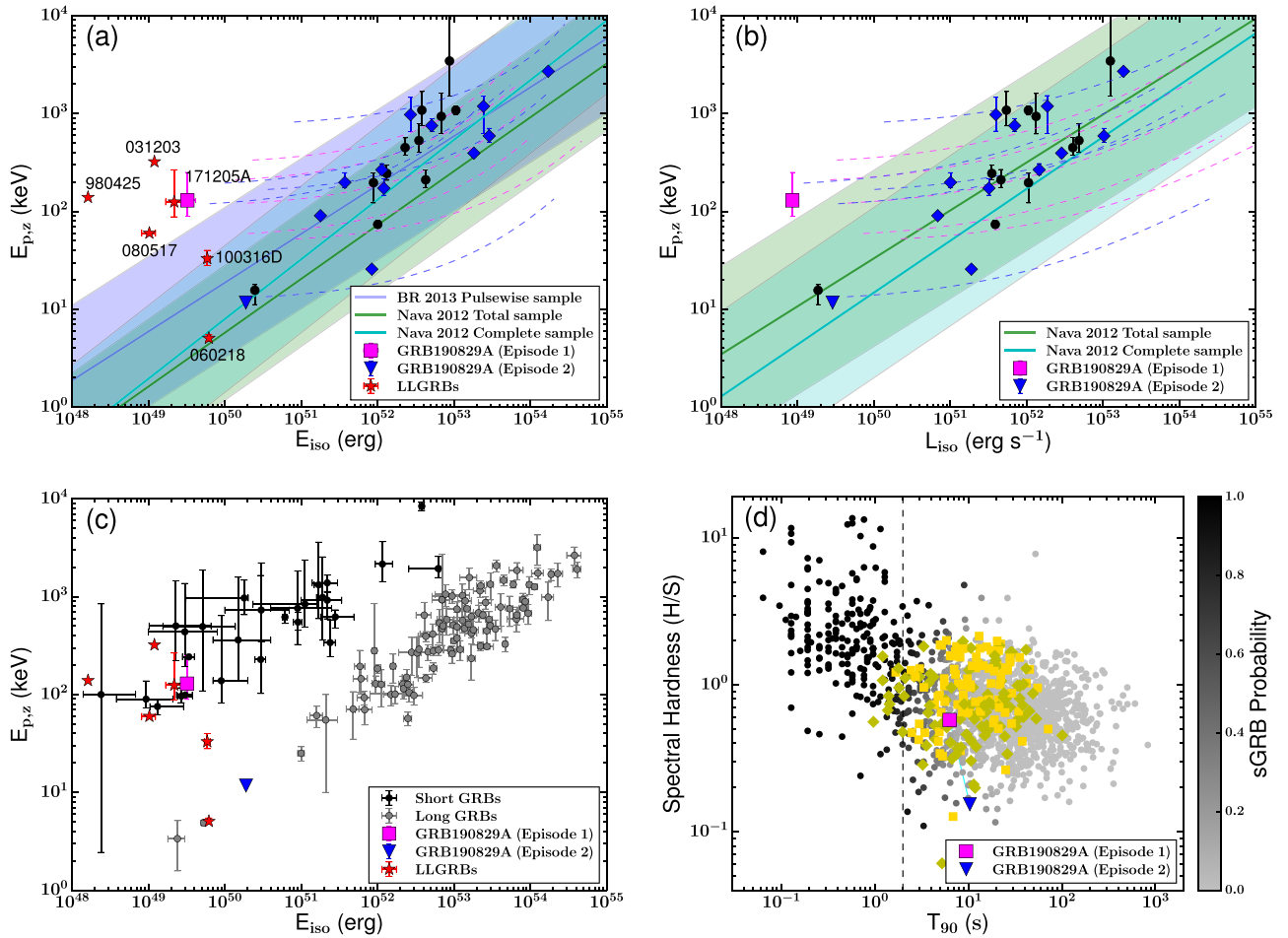


Figure 2. Correlations for two-episode GRBs: the first episodes (black circles) and second episodes (blue diamonds) of two-episode long GRBs with known redshifts in (a) the Amati and (b) the Yonetoku correlation plane. GRBs with unknown redshifts are represented by tracks obtained by varying the redshift (for all the tracks, see the Appendix). The shaded region represents the 3σ scatter of the correlations (Nava et al. 2012; Basak & Rao 2013). The two episodes of GRB 190829A are shown with colored symbols. (c) The two episodes of GRB 190829A in the Amati correlation plane of long and short GRBs. (d) The spectral hardness and duration T_{90} for the two-episode GRBs shown along with the data points for short (black circles) and long GRBs (gray circles) used in Goldstein et al. (2017). Gold squares and yellow diamonds represent the first and second episodes of two-episode long GRBs with known redshifts, respectively. The color scale represents the probability of a GRB being short (black) or long (gray).

Figure 2(d), we show the HR- T_{90} diagram of the two-episode GRBs, with each episode considered separately. The probabilities of a GRB classified as a short or long GRB from the Gaussian mixture model in the logarithmic scale are also shown in the background (taken from Goldstein et al. 2017). We note that all these data are clustered toward the long GRB category. The probability of the first episode being associated with long GRB properties is $\sim 87\%$.

Long GRBs show soft lag where the light curve in the low-energy band lags behind the light curve in the high-energy band (Fenimore et al. 1995), however, many short GRBs do not show a statistically significant lag (Bernardini et al. 2015). We calculate the spectral lags for GRB 190829A using the discrete cross-correlation function (CCF) as defined in Band (1997). The peak of the observed CCF versus spectral lag is found by fitting an asymmetric Gaussian function (Bernardini et al. 2015). The lags are calculated between 150–300 keV and the lower energy bands (8–30 keV and 8–100 keV), and the values are reported in Table 1. The upper value of energy is restricted to 300 keV because the signal above this energy is consistent with the background. We chose light curves of different resolutions (4, 8, and 16 ms), and the maximum correlation is obtained for 8 ms. The lags with energy bands and the

maximum value of correlations are reported in Table 1. A positive lag is obtained for both episodes, and it is consistent with the soft lags generally seen in long GRBs.

This analysis through the properties in the HR versus the T_{90} diagram and a positive spectral lag for both episodes strongly suggests that GRB 190829A is consistent with the population of long GRBs through the contrasting nature of its episodes in the prompt emission energy correlations.

3. Multiwavelength Modeling

3.1. H.E.S.S. and Fermi-LAT Observations

We extracted the LAT data within a temporal window extending 50,000 s after T_0 . We performed an unbinned likelihood analysis. The data were filtered by selecting photons with energies in the range 100 MeV–300 GeV, within a region of interest of 12° centered on the burst position. A further selection of zenith angle (100°) was applied in order to reduce the contamination of photons coming from the Earth limb. We adopted the P8R3_SOURCE_V2 response, which is suitable for longer durations ($\sim 10^3$ s). The probability of the photons to be associated with GRB 190829A is calculated using the `gtsrcprob` tool.

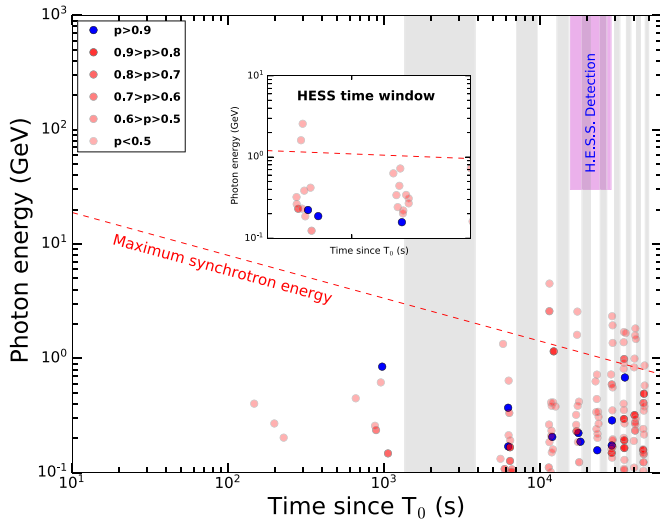


Figure 3. Delayed emission in LAT: all the photons with energies >100 MeV and probabilities of being associated with GRB 190829A. The regions with zenith angle $>100^\circ$ are shaded gray. The red line represents the maximum photon energies allowed for a synchrotron forward-shock model with an emission efficiency $\eta = 1.3\%$. The inset shows the LAT emission during the H.E.S.S. time window.

We analyzed Fermi-LAT data up to 5×10^4 s after the GBM trigger time, see Figure 3. We obtained an upper limit on photon flux of 2.81×10^{-7} photons $\text{cm}^{-2} \text{s}^{-1}$ in 100 MeV–300 GeV. Fermi-LAT detected no photons during the GBM observation, which is consistent with the extrapolated Comptonized spectrum peaking at ~ 114 keV (see Table 1). During the H.E.S.S. observation, which started 4.2 hrs after the prompt emission, only three photons are observed in the LAT above 100 MeV with a probability $>90\%$ of their association with the source, though more photons are observed with $>50\%$ probability.

To investigate the origin of the LAT photons, we calculated the maximum photon energy radiated by the synchrotron process during the deceleration phase (Piran & Nakar 2010; Barniol Duran & Kumar 2011; Fraija et al. 2019a). The red dashed line represents the maximum photon energies released by the synchrotron forward-shock model with an emission efficiency of prompt emission $\sim \eta = 1.3\%$ (Section 3.2.2). The LAT photons lying below this line are consistent with synchrotron emission. However, the H.E.S.S. detection would lie above this line and might originate from the synchrotron self-Compton mechanism similar to GRB 190114C and GRB 180720B (MAGIC Collaboration et al. 2019b; Abdalla et al. 2019).

3.2. X-Rays and Optical Data

The Swift XRT (Burrows et al. 2005) began observing the BAT localization field to search for an X-ray counterpart of GRB 190829A at 19:58:21.9 UT, 97.3 s after the BAT trigger. The XRT detected a bright and uncataloged X-ray afterglow candidate at R.A. (J2000) and decl. (J2000) of $02^{\text{h}} 58^{\text{m}} 10^{\text{s}}.57$ and $-08^{\circ} 57' 28''.6$, respectively, with a 90% uncertainty radius of $2''.0$. This position was within the Swift-BAT error circle (Dichiara et al. 2019). Subsequently, the Ultra-Violet and Optical Telescope (UVOT) on board Swift, and many ground-based optical and NIR telescopes, began to follow-up observations of the GRB. We summarize these observations and also reduce data for the present analysis.

3.2.1. Observations and Data Reduction

The X-ray afterglow was monitored until $\sim 7.8 \times 10^6$ s post-trigger beginning with the window timing mode. Finally, upper limits are obtained with photon-counting mode (PC) data at 1.02×10^7 s (~ 4 months). The XRT light curve and the spectrum have been obtained from the Swift online repository¹⁶ hosted by the University of Leicester (Evans et al. 2007, 2009). The UVOT observed the source position 106 s after the BAT trigger (Dichiara et al. 2019). An optical counterpart candidate consistent with the X-ray afterglow position had been discovered (Oates & Dichiara 2019). We obtained UVOT data from the Swift archive page.¹⁷ For the UVOT data reduction, we used HEASOFT software v6.25 with the latest calibration database. We performed the reduction of the UVOT data using the *uvotproduct* pipeline. A source circular region of $5''$ and a background region of $25''$ aperture radius were extracted for the analysis. All the magnitudes have been converted to flux density using the UVOT zero-point flux.¹⁸ Correction for Galactic and host galaxy extinction is not applied. Results are plotted in Figure 4(b) and reported in Table A2.

An evolving optical counterpart with preliminary magnitude $m(r) \sim 16.0$ was reported by Xu et al. (2019) using the Half Meter Telescope. Valeev et al. (2019) observed the optical afterglow using the 10.4 m Gran Telescopio Canarias. A red continuum with the Ca, H, and K doublet absorption line was detected in the afterglow spectrum along with the emission lines of the SDSS galaxy (J025810.28-085719.2) at redshift $z = 0.0785$. Other ground-based optical and NIR telescopes also observed this evolving source in various filters (Blazek et al. 2019; Chen et al. 2019; D’Avanzo et al. 2019; Fong et al. 2019; Heintz et al. 2019; Kumar et al. 2019; Lipunov et al. 2019a; Paek & Im 2019; Perley & Cockeram 2019a, 2019b; Strausbaugh & Cucchiara 2019; Vagnozzi & Nesci 2019; Zheng & Filippenko 2019). We applied the Galactic extinction correction from the observed magnitudes using Schlafly & Finkbeiner (2011). An associated supernova also has been reported by using photometry and spectroscopy observations (Bolmer et al. 2019; Lipunov et al. 2019b; Perley & Cockeram 2019c, 2019d; Terreran et al. 2019; de Ugarte Postigo et al. 2019b; Volnova et al. 2019).

The combined multiwavelength light curves are shown in Figure 4. For completeness, we also showed low-frequency data points (Chandra 2019; Monageng et al. 2019; Laskar et al. 2019; de Ugarte Postigo et al. 2019a). Through visual inspection, we can note that the optical flare is correlated with the X-ray flare.

3.2.2. Analysis

We have analyzed the XRT spectrum in the 0.3–10 keV band in XSPEC. We used an absorption component along with the source spectral model. For this component, we chose a fixed Galactic column density of $5.60 \times 10^{20} \text{ cm}^{-2}$, and a free intrinsic column density for the host redshift of 0.0785. We consider two models, a simple power-law model and a broken-power-law model (bknpow). We also searched for additional thermal and other possible components, however, such components are not present or not preferred by statistics. With each model, we included XSPEC models *phabs* and *zphabs* for Galactic and

¹⁶ <https://www.swift.ac.uk/>

¹⁷ <http://swift.gsfc.nasa.gov/docs/swift/archive/>

¹⁸ <http://svo2.cab.inta-csic.es/theory/fps3/index.php?mode=voservice>

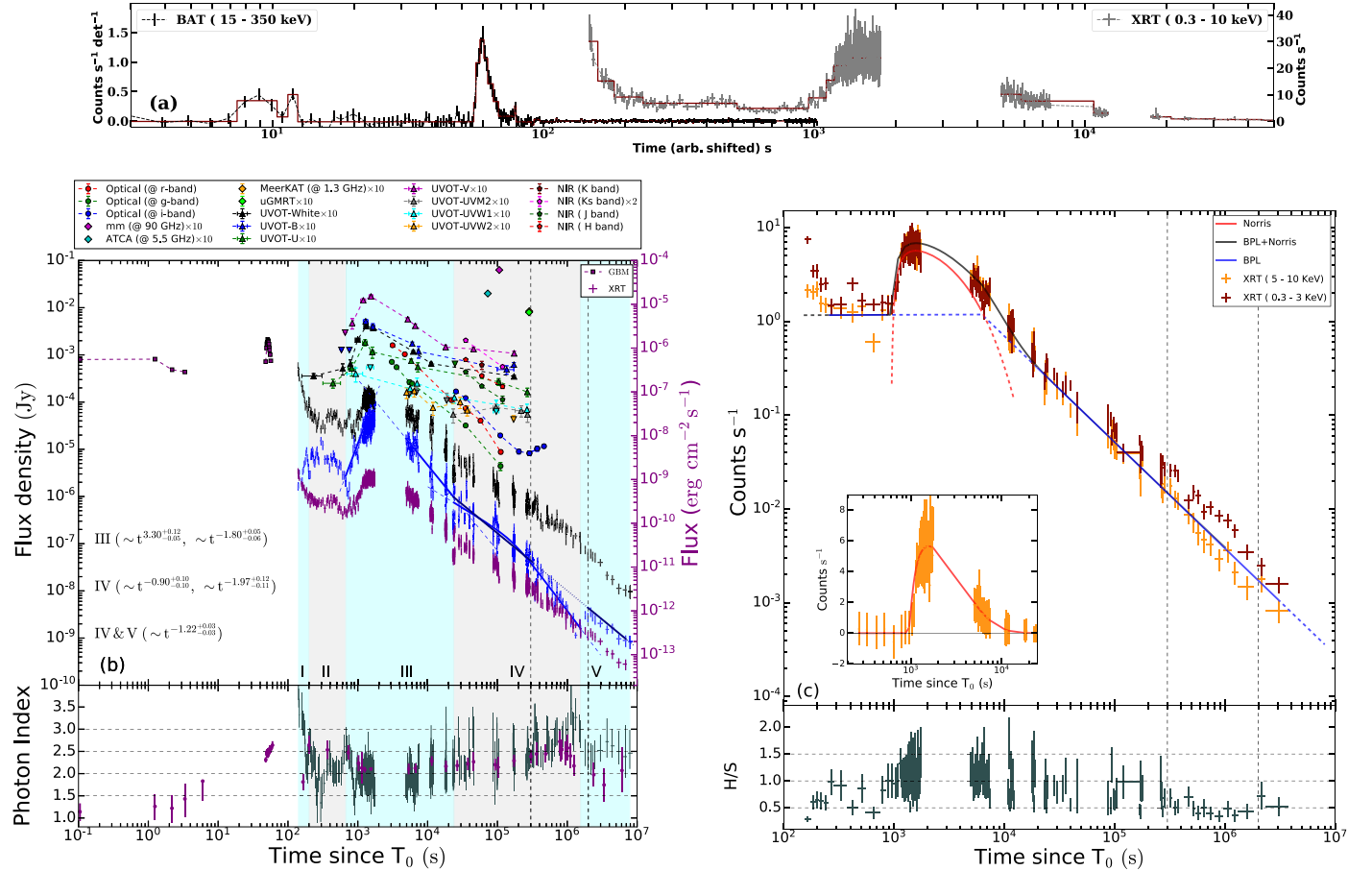


Figure 4. Multiwavelength light curves. (a) BAT and XRT observation of all the episodes in log-linear scale. (b) Upper panel: flux ($\text{erg cm}^{-2} \text{s}^{-1}$) for GBM (10–1000 keV) and XRT (0.3–10 keV) labeled on the right axis (purple axis), whereas the left axis shows the flux density (Jy) in different wavelength regimes. The down-pointing triangles denote the corresponding upper limits. For XRT, black data points are flux density @ 1 keV and blue data points are flux density @ 10 keV. The shaded regions show the different episodes selected, and data between the vertical black dashed lines is ignored for modeling and is a possible rebrightening region. Lower panel: photon index. (c) XRT light curves. Upper panel: XRT count rate in the hard (5–10 keV) and soft (0.3–3 keV) bands. The figure in the inset shows the background-subtracted flaring episode fitted well by the Norris model. Lower panel: the ratio of the count rate in hard and soft bands (HR). The vertical black dashed lines are the same as in (b). All XRT data are taken and reduced from the Swift online repository (Evans et al. 2009).

intrinsic absorption, respectively. We also included the `redden` and `z dust` models for interstellar extinction and reddening in the host, respectively. We considered Milky Way, LMC, and SMC extinction laws to get the reddening in the host. All the parameters, along with various models, have been shown in Table 2.

We divide the XRT flux light curve into five phases (numbered I to V) based on its evolution. The initial emission in the X-rays shows different decay behavior in flux and flux density (@ 10 keV). The flux decays with an index ~ 3 while the flux density (@ 10 keV) shows a sporadically changing behavior in the beginning. This is also reflected in our joint analysis of XRT and BAT data for phase I where we found that the spectrum could be described by a cutoff power-law model. The spectral index as shown in the lower panel is also varying fast during phase I. A strong flare is also present in both X-ray, Swift-UVOT and optical light curves beginning from ~ 600 s. We have modeled the X-rays in phase I by a power law, and III and IV by a power law with a smooth break. The measured spectral and temporal parameters of the XRT light-curve fitting are shown in Tables 2 and 3.

The external shock models predict certain closure relations between the spectral and temporal index in various regimes

(cooling, density regimes, or an injection from the central engine). These relations present tests without delving into details of the models (e.g., Zhang & Mészáros 2004; Gao et al. 2013). Using the conventional notation, $F_\nu \propto t^{-\alpha} \nu^{-\beta}$, we obtained α_X , β_X for GRB 190829A afterglow in the X-ray bands. In Table 3, we present the indices of the flux and flux density (@ 10 keV) for the segments of the light curve. We particularly analyze segments III (flare) and IV (break) regions in detail, starting with phase IV.

The segment in the flux light curve shows a shallow change (0.3 ± 0.3) in the temporal decay index. Contrary to this, in the flux density (@ 10 keV), α_X changes by 1.1 ± 0.2 . Naively, one may tend to recognize the break with a jet break, however, upon closer examination the photon index softens during $\sim 3 \times 10^5$ – 2×10^6 s (vertical dashed lines in Figure 4(b)). This is also reflected in the softening of the hardness ratio (vertical dashed lines in Figure 4(c)). Since after this period, the photon index settles down to its previous value before the spectral change, it suggests a rebrightening within the low-energy Swift-XRT band. The passage of some spectral break frequency is also less likely due to the same reason, because any frequency crossover will cause an irreversible change in the spectral index. Phases IV and V (excluding the

Table 3
The Best-fit Values of Spectral and Temporal Indices for Episodes Marked in Figure 4

X-Rays	Intervals (s) from Flux (erg cm ² s ⁻¹)	Index α	$-\log(L)/(n, k)$	Index β	Intervals (s) from Flux @ 10 keV (Jy @ 10 keV)	Index (α_X)	$-\log(L)/(n, k)$	Index (β_X)
I	89.54–147.93	$2.99^{+0.20}_{-0.30}$	362/(16, 3)	$1.18^{+0.26}_{-0.24}$
II	147.93–619.84	$1.46^{+0.23}_{-0.22}$
III	$619.84-2.37 \times 10^4$ $t_b = 1570^{+68}_{-67}$	$-2.82^{+0.18}_{-0.20}$ $1.43^{+0.05}_{-0.05}$...	$1.02^{+0.06}_{-0.06}$ $1.05^{+0.09}_{-0.09}$	620–1140 $4860-2.37 \times 10^4$	$-3.30^{+0.12}_{-0.05}$ $1.80^{+0.05}_{-0.05}$	584/(49, 3) 1988/(155, 3)	$1.18^{+0.22}_{-0.21}$ $1.01^{+0.09}_{-0.09}$
IV	$2.37 \times 10^4-9.60 \times 10^5$ $t_b = 3.95^{+2.39}_{-1.28} \times 10^5$	$1.02^{+0.03}_{-0.03}$ $1.33^{+0.13}_{-0.29}$...	$1.13^{+0.09}_{-0.09}$ $1.32^{+0.25}_{-0.24}$	$2.37 \times 10^4-1.55 \times 10^6$ $t_b = 1.67^{+0.4}_{-0.3} \times 10^5$	$0.90^{+0.10}_{-0.10}$ $1.97^{+0.12}_{-0.11}$...	$1.02^{+0.12}_{-0.11}$ $1.35^{+0.13}_{-0.13}$
IV – V ^b	$9.60 \times 10^5-7.90 \times 10^6$	$1.1^{+0.1}_{-0.1}$	4031/(154, 3)	$1.05^{+0.28}_{-0.26}$	$2.37 \times 10^4-6.87 \times 10^6$	$1.22^{+0.03}_{-0.03}$	2468/(155, 3)	$1.21^{+0.1}_{-0.1}$

Notes. We use a power-law or a smooth-broken-power-law^a function to model the XRT light curves for different segments using the *python* module *emcee* (Foreman-Mackey et al. 2013). All quoted errors on spectral parameters correspond to the 16th and 84th percentiles.

^a

$$\text{Flux} \propto \left[\left(\frac{t}{t_b} \right)^{\alpha_1 s} + \left(\frac{t}{t_b} \right)^{\alpha_2 s} \right]^{-1/s}$$

s : smoothness parameter, α_1 : index before break t_b , α_2 : index after break (Wang et al. 2018), $\log(L)$: log-likelihood, n : number of data points, and k : number of the free parameters in the fit.

^b Excluding $3 \times 10^5-2 \times 10^6$ s.

region between the black dashed lines) is consistent with a typical decay with $\alpha_X \sim 1.22 \pm 0.03$. The UVOT data in this phase is possibly dominated by the contribution of the host. The observation in the *i*-band shows the rising part of a supernova (Perley & Cockeram 2019c) contemporaneous with the break t_b .

Consider adiabatic cooling without energy injection from the central engine. The inferred value of α_X (1.31 ± 0.15) from observed β_X (1.21 ± 0.1) matches with the observed value (1.22 ± 0.03) within error bars for the spectral regime $\nu > \nu_c$ and the interstellar or Wind mediums (Table 3). We estimate the value of the electron distribution index $p = 2.42 \pm 0.2$ from $p = 2\beta$. We calculate the kinetic energy in the jet $E_{K,iso} = 1.7 \times 10^{52}$ erg according to Equation (17) of Wang et al. (2015), which is valid for the case $\nu_X > (\nu_m, \nu_c)$. We took a prebreak segment from phase IV (0.27–1.9 days) with a mean photon arrival time ~ 0.7 day. The following values of the parameters are assumed: the fraction of postshock thermal energy in magnetic fields $\epsilon_B = 0.1$, in electrons $\epsilon_e = 0.1$, and from the spectrum of this segment $p = 2.6$; negligible inverse-Compton scattering and the typical value of ambient number density $n = 1 \text{ cm}^{-3}$ (Racusin et al. 2009; Wang et al. 2018). The efficiency (η) is then calculated by the ratio of the isotropic radiation emitted in the prompt emission and the total energy $E_{\gamma,iso}/(E_{\gamma,iso} + E_{K,iso})$. The efficiency η is $\sim 1.3 \times 10^{-2}$ ($\sim 1.3\%$).

3.3. X-Ray Flares

Other than the two episodes detected in the prompt emission, we observed flaring activities in the X-ray afterglows. The average photon index in the nonflaring region scatters around the mean value near to the BAT photon index. For the flaring regions, e.g., the initial phase I, it has an altogether different spectrum (CPL), and the same is reflected in a softer photon index. The softer and fast-varying spectrum here is in support of the flaring activity. To uncover this, in the right panel (Figure 4(c)), we have plotted the count-rate light curve in a low- and high-energy band, optimized to see this effect, and we show that there is a flaring activity in the low energies. The spectra for the phases as well as Bayesian blocks obtained from the count-rate light curve in 0.3–10 keV are

fit, and the photon indices are plotted in the lower panel of Figure 4(b). The photon index also scatters only about the mean values we have found for different phases. Some trending variations (the region between the black dashed lines) are as a result of possible low-energy rebrightening.

Most prominent among the X-ray flares is phase III. The initial decaying phase (I) has a cutoff in the spectrum. The spectral index (plotted in the second panel of Figure 4(b)) varies fast during phases I and II and, therefore, there are flare-like activities. Episode III is a larger flare with a fast rise and decays with an index of ~ 2 . We discuss two scenarios for the origin of this flare.

(a) *Reverse-shock emission in an external shock*: the origin of flared emission can also be due to the reverse-shock propagation into the ejecta medium (Kobayashi et al. 2007; Fraija et al. 2017). Since the X-ray flare is much delayed from the prompt phase, reverse shock occurs in a thin shell. The predicted temporal index for reverse-shock synchrotron self-Compton (SSC) emission before the peak is $\alpha_X = 5(1-p)/4$ and after the peak is $\alpha_X = (3p + 1)/3$. Using the observed values for phase III, we estimate $p = 3.64^{+0.04}_{-0.09}$ and $p = 1.47 \pm 0.05$ before and after the peak, respectively. Clearly, the reverse-shock SSC emission is not a consistent interpretation.

(b) *Late-time central-engine activity*: giant flares have been detected in X-rays and are associated with the central-engine activity (Falcone et al. 2006; Dai & Liu 2012; Gibson et al. 2017). These flares are superimposed on the underlying afterglow emission. We have plotted count-rate light curves for hard (H: 5–10 keV) and soft (S: 0.3–1.5 keV) bands in Figure 4(b). The hardness ratio (H/S) is shown in the lower panel of Figure 4 which reflects the comparative strength of the signal in these two bands. This uncovers a plateau phase before the flare in the H band. The peak rate of the flare beginning at ~ 1000 s is ~ 5.8 times higher in comparison to the plateau phase. We model the overall light curve using a combination of a broken power law for the underlying afterglow and a Norris model¹⁹ for the flare (Norris et al. 2005). We calculate the pulse width (w) and

¹⁹ $I(t) = A \exp[-\tau_1/(t - t_i) - (t - t_i)/\tau_2]$, where A is pulse amplitude, τ_1 and τ_2 are rise and decay time of the pulse, respectively, and t_i is the start time. The fit parameters are $A = 5.6 \pm 0.2$, $\tau_1 = 161^{+61}_{-46}$, $\tau_2 = 2742^{+250}_{-280}$, and $t_i = 909^{+33}_{-41}$. The pulse width is $w = \tau_2(1 + 4\sqrt{\tau_1/\tau_2})^{0.5}$. The rise time $t_r \sim 553$ s, decay-time rise time is $t_d \sim 3293$ s, and peak time t_{pk} is 1573 s.

asymmetry of the pulse using the measured values of pulse rise and decay time and find that w is ~ 3848 s and the asymmetry k using the relation ($k = \tau_2/w$) is 0.71. The ratio of rise time (t_r) to decay time (t_d) is ~ 2 and is well within the t_r/t_d distribution. The origin of the X-ray flares (bumps observed in X-ray emission) in GRBs is widely discussed and studied (Ioka et al. 2005; Curran et al. 2008; Chincarini et al. 2010). Among the X-ray flares observed, the late-time flares (with $t_{pk} \sim 1000$ s) are also specifically studied (Curran et al. 2008; Bernardini et al. 2011). The relative variability defined as w/t_{pk} is ~ 2.4 . This implies the kinematically allowed regions in the “Ioka plot” for the X-ray flare in GRB 190829A are where the emission is originating from refreshed shocks or patchy shells, and this does not satisfy the general requirement ($w/t_{pk} < 1$) for an internal activity (Ioka et al. 2005; Curran et al. 2008; Chincarini et al. 2010; Bernardini et al. 2015). The isotropic X-ray energy $E_{X,iso}$ of the flaring phase is 4.49×10^{49} erg.

4. Summary and Discussion

In this paper, we highlighted the unusual spectral features of episodic activities in GRB 190829A from the prompt emission to afterglows. We found that Amati and Yonetoku relations are satisfied for GRBs with multiple episodes separated by quiescent phases. But, the first episode of GRB 190829A is the only outlier. It also does not satisfy the pulse-wise Amati correlation known for well-separated individual pulses of GRBs (Basak & Rao 2013). In the hardness-duration diagram and spectral lags, this GRB emission is consistent with long GRBs (Narayana Bhat et al. 2016; Goldstein et al. 2017).

Shock breakout origin of the prompt emission? Some of the low-luminosity GRBs are not compatible with the Amati correlation (see Figure 2). The radiation in LLGRBs is powered by shock breakout and the energetics satisfy a fundamental correlation $T_{90} \sim 20 \text{ s} (1+z)^{-1.68} \left(\frac{E_{\gamma,iso}}{10^{46} \text{ erg}} \right)^{1/2} \left(\frac{E_p}{50 \text{ keV}} \right)^{-2.68}$ (Nakar & Sari 2012). For the parameters of the first episode which lies outside in the Amati plane (3σ), $E_{\gamma,iso} \sim 3.2 \times 10^{49}$ erg and $E_p \sim 120$ keV, and $z = 0.0785$, the predicted shock breakout duration is ~ 9.5 s which is similar to T_{90} or the duration of the episode taken for spectral analysis (~ 8.7 s). This is favorable evidence for the shock breakout interpretation of this episode. For the second episode considering $E_p = 10$ keV, the predicted T_{90} is > 18135 s. This is much larger than the observed value of 10.4 s for a shock breakout, we do not expect this variability on a scale much shorter than the typical timescale of the pulse (e.g., the rise time ~ 1 s in the case of GRB 190829A). From the Bayesian blocks (Scargle et al. 2013) constructed for the GBM–NaI and the BAT light curves, we found that no -time variability is found (with a false-alarm probability $p_0 = 0.35$). The observed prompt emission efficiency is $\eta \sim 1.3\%$ which is normal as observed for long and short GRBs (Zhang et al. 2007; Racusin et al. 2011) and not low ($\sim 10^{-4}$) as observed for shock breakout and LLGRBs (Gottlieb et al. 2018). The soft episode is separated from the low-luminosity hard episode by a quiescent phase, and has a spectrum which is a power law with value typically observed for a Band high-energy power-law spectrum in GRBs. This is contrary to the soft thermal emission with no significant gap expected in the shock breakout model. A shock breakout interpretation would also raise the upper limit of the shock breakout luminosity by ~ 10 times the previous limit of 10^{48} erg s^{-1} (Zhang et al. 2012) and the critical limit set in Matsumoto & Piran (2020). Hence, our analysis suggests that emission in GRB 190829A is not caused by a shock breakout.

The late-time flare observed is unusual as the relative variability is atypical and the flare is also observed simultaneously in optical bands. A similar example with $w/t_{pk} > 1$ is GRB 050724 which was extensively studied. Detailed studies showed that the flare in GRB 050724 could be interpreted within different frameworks (Panaitescu 2006; Malesani et al. 2007; Lazzati & Perna 2007; Bernardini et al. 2011). Another possibility for the origin of the flare includes fallback accretion on a newborn magnetar (Gibson et al. 2017).

In late-time LAT emission, there are some photons (> 100 MeV) associated with the source, which may have originated in synchrotron emission as GRB 190114C and the H.E.S.S. detection, which lies above the maximum synchrotron energy and similarly might have inverse-Compton emission. The X-ray observations during the flare emission, which occurs after 1000 s, cannot be explained by the reverse-shock SSC temporal relations (Kobayashi et al. 2007; Fraija et al. 2017). An excess emission in the energy X-ray band (0.3–3 keV) is seen at times $\sim 3 \times 10^5$ – 2×10^6 s and softening is observed in the HR during this. The time-averaged γ -ray luminosity for GRB 190829A is one order of magnitude above the threshold for internal engine activity ($\sim 10^{48}$ erg s^{-1}), which disfavors shock breakout origin (Zhang et al. 2012). Given the detection in the teraelectronvolt band, it is likely that the viewing angle is closer to the jet axis, as larger viewing angles may not provide sufficient Doppler boosting. This implies it is the faintness of GRB episodes that is intrinsic rather than the effect of the viewing angle. The early signature of an emerging supernova emission in optical i -band, as shown in Figure 4(a), further supports this hypothesis. However, a deeper understanding would require incorporating detailed modeling of the source, including the H.E.S.S. observation and the study of the associated supernova.

We thank Dr. K.L. Page and Dr. Phil Evans of the Swift helpdesk for helpful discussions to deal with Swift-XRT data. We thank Professor Bing Zhang for a discussion on the possible interpretation of the results. We also thank Professor A.R. Rao, Dr. Gor Oganessian, Dr. A. Tsvetkova, and Dr. N. Fraija for fruitful discussions. We are thankful to Dr. P. Veres for sharing data related to Figure 2(d). We also acknowledge and are thankful for the constructive comments by the anonymous referee. This work is supported by the National Key Research and Development Programs of China (2018YFA0404204), the National Natural Science Foundation of China (grant No. 11833003), and the Innovative and Entrepreneurial Talent Program in Jiangsu, China. B.B.Z. acknowledges support from a national program for young scholars in China. R.G. and S.B.P. acknowledge BRICS grant DST/IMRCD/BRICS/PilotCall1/ProFCheap/2017(G). P.S.P. acknowledges SYSU-Postdoctoral Fellowship. R.B. acknowledges funding from the European Union’s Horizon 2020 research and innovation program under the Marie Skłodowska-Curie grant agreement No. 664931. This research has made use of data obtained through the HEASARC Online Service, provided by the NASA-GSFC, in support of NASA High Energy Astrophysics Program.

Appendix Two-phase GRBs with Redshift Detection

For the sample of GRBs with two episodes, as reported in Lan et al. (2018), 11 have measured redshift.²⁰ We extracted

²⁰ <http://www.mpe.mpg.de/~jcg/grbgen.html>

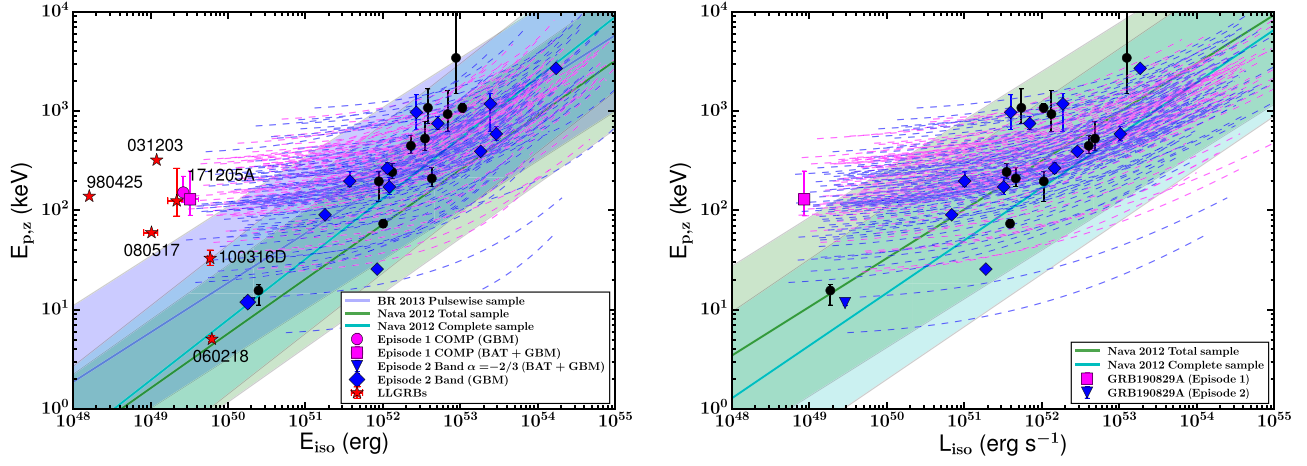


Figure A1. Correlations for two-episode GRBs: same as Figure 2. Tracks for all the GRBs without redshift are shown. A BAT + GBM data point is shown for episode 1. For episode 2, the low-energy index ($\alpha = -2/3$) is set to the slow cooling limit.

Table A1
Bursts with Two-episode Emission and Redshift Detection

Trigger ID	z	$T_{\text{Ep},1}$ $T_{\text{Ep},2}$ (s)	T_q (s)	$F_{\text{Ep},1}$ $F_{\text{Ep},2}$	$F_{\text{peak},1}$ $F_{\text{peak},2}$	$E_{p,1}$ $E_{p,2}$ (keV)	α_1 α_2	$E_{\text{iso},1}$ $E_{\text{iso},2}$	$L_{\text{iso},1}$ $L_{\text{iso},2}$	Model _{Ep,1} Model _{Ep,2}
bn090328401	0.736	36.68 18.36	...	$1.949^{+0.136}_{-0.138}$ $0.117^{+0.018}_{-0.014}$	$4.290^{+0.862}_{-0.287}$ $0.410^{+0.092}_{-0.104}$	655^{+78}_{-65} 96^{+32}_{-17}	$-0.96^{+0.03}_{-0.03}$ $+1.26^{+0.19}_{-0.21}$	10.62 0.37	1.054 0.101	Band COMP
bn091208410	1.063	4.33 5.85	...	$0.392^{+0.051}_{-0.041}$ $0.656^{+0.052}_{-0.045}$	$0.751^{+0.153}_{-0.105}$ $2.381^{+0.193}_{-0.167}$	102^{+28}_{-17} 129^{+20}_{-15}	$+1.19^{+0.17}_{-0.19}$ $+1.15^{+0.10}_{-0.10}$	4.27 1.14	0.461 1.461	COMP COMP
bn100615083	1.398	25.51 18.37	...	$0.369^{+0.084}_{-0.066}$ $0.130^{+0.016}_{-0.013}$	$0.869^{+0.209}_{-0.184}$ $0.264^{+0.062}_{-0.047}$	86^{+18}_{-31} 72^{+17}_{-11}	$-1.10^{+0.29}_{-0.13}$ $-1.35^{+0.16}_{-0.18}$	0.89 1.21	1.058 0.321	Band COMP
bn111228657	0.714	37.76 20.39	...	$0.259^{+0.027}_{-0.024}$ $0.284^{+0.017}_{-0.017}$	$1.705^{+0.268}_{-0.197}$ $0.830^{+0.095}_{-0.051}$	48^{+4}_{-4} 15^{+1}_{-1}	$-1.63^{+0.07}_{-0.07}$ $+0.41^{+3.70}_{-1.35}$	1.01 0.84	0.389 0.189	Band Band
bn120711115	1.405	10.20 65.16	...	$0.354^{+0.163}_{-0.104}$ $5.160^{+0.105}_{-0.133}$	$1.079^{+0.982}_{-0.381}$ $15.075^{+1.842}_{-1.607}$	389^{+278}_{-131} 1123^{+58}_{-88}	$+0.41^{+0.42}_{-0.62}$ $-0.95^{+0.02}_{-0.01}$	6.85 172.27	1.329 18.576	COMP Band
bn120716712	2.486	7.14 47.95	...	$0.236^{+0.051}_{-0.036}$ $0.263^{+0.034}_{-0.024}$	$0.957^{+0.125}_{-0.123}$ $0.568^{+0.085}_{-0.046}$	152^{+74}_{-37} 113^{+10}_{-11}	$+1.10^{+0.21}_{-0.26}$ $-0.87^{+0.11}_{-0.09}$	3.49 18.30	4.841 2.873	COMP Band
bn131108024	2.400	12.24 54.09	...	$0.236^{+0.031}_{-0.024}$ $0.176^{+0.084}_{-0.035}$	$0.868^{+0.161}_{-0.129}$ $0.403^{+0.250}_{-0.112}$	132^{+34}_{-22} 410^{+133}_{-139}	$+1.03^{+0.17}_{-0.19}$ $-0.46^{+0.35}_{-0.23}$	2.30 24.44	4.028 1.870	COMP Band
bn140304849	5.283	36.74 70.40	...	$0.146^{+0.034}_{-0.038}$ $0.084^{+0.009}_{-0.008}$	$0.404^{+0.160}_{-0.100}$ $0.333^{+0.091}_{-0.069}$	548^{+1043}_{-307} 94^{+18}_{-13}	$+1.41^{+0.13}_{-0.19}$ $+1.03^{+0.18}_{-0.16}$	8.78 29.07	12.476 10.284	COMP COMP
bn140512814	0.725	13.25 67.27	...	$0.756^{+0.121}_{-0.103}$ $0.555^{+0.054}_{-0.045}$	$2.297^{+0.710}_{-0.648}$ $2.941^{+0.778}_{-0.516}$	627^{+344}_{-192} 436^{+78}_{-59}	$+1.09^{+0.06}_{-0.07}$ $+1.16^{+0.04}_{-0.04}$	3.81 5.12	0.544 0.696	COMP COMP
bn151027166	0.810	25.50 31.62	...	$0.209^{+0.021}_{-0.016}$ $0.497^{+0.092}_{-0.078}$	$1.125^{+0.097}_{-0.098}$ $1.270^{+0.631}_{-0.349}$	135^{+29}_{-20} 538^{+271}_{-173}	$+1.31^{+0.11}_{-0.11}$ $+1.42^{+0.05}_{-0.07}$	1.32 2.71	0.351 0.396	COMP COMP
bn180728728	0.117	4.08 9.02	...	$0.313^{+0.044}_{-0.041}$ $6.392^{+0.012}_{-0.010}$	$0.536^{+0.081}_{-0.091}$ $19.794^{+0.522}_{-0.501}$	14^{+2}_{-4} 81^{+1}_{-1}	$+0.21^{+0.98}_{-1.98}$ $-1.53^{+0.01}_{-0.01}$	0.02 0.18	0.002 0.068	Band Band

Note. $F_{\text{Ep},1}$, $F_{\text{Ep},2}$, $F_{\text{peak},1}$, and $F_{\text{peak},2}$ are in units of $10^{-6} \text{ erg cm}^{-2} \text{ s}^{-1}$; $E_{\text{iso},1}$ and $E_{\text{iso},2}$ are in units of 10^{52} erg ; $L_{\text{iso},1}$ and $L_{\text{iso},2}$ are in units of $10^{52} \text{ erg s}^{-1}$.

the spectrum using the same criteria as described in Section 2 and performed time-integrated analysis for each episode. We fit COMP and Band models to the background-subtracted spectral data and compared the models using the BIC. For studying correlations, we calculated the flux within the energy range specified by $1/(1+z) \text{ keV}$ to $10/(1+z) \text{ MeV}$ and computed the E_{iso} and L_{iso} . The results are reported in Table A1. For other

GRBs in the sample, spectral properties of each episodes are well constrained but there is no redshift estimate. Here we calculated the E_{iso} and L_{iso} values by varying redshift ranging from 0.01 to 10 shown by continuous tracks in Figure A1. We assume the following cosmology parameters: Hubble parameter $H_0 = 71 \text{ km s}^{-1} \text{ Mpc}^{-1}$, total matter density $\Omega_M = 0.27$, and dark energy density $\Omega_\Lambda = 0.73$.

Table A2

Log of UVOT Observations and Photometry of the GRB 190829A Afterglow

Filter	T_i (s)	T_s (s)	Magnitude	Flux Density (mJy)
white	106.3	256.1	19.51 ± 0.14	0.036 ± 0.005
white	545.8	565.6	19.12 ± 0.29	0.051 ± 0.014
white	721.6	741.3	18.87 ± 0.24	0.064 ± 0.014
white	870.6	1020.0	17.57 ± 0.04	0.213 ± 0.008
white	1173.5	1366.5	16.88 ± 0.06	0.401 ± 0.022
white	1519.3	1701.6	16.96 ± 0.08	0.373 ± 0.027
white	6079.3	6279.0	18.21 ± 0.05	0.118 ± 0.005
white	10724.2	11631.1	18.85 ± 0.04	0.065 ± 0.002
white	17223.6	173130.6	19.53 ± 0.06	0.035 ± 0.002
<i>b</i>	521.3	541.1	>18.76	>0.127
<i>b</i>	696.3	716.1	>18.76	>0.127
<i>b</i>	1148.7	1342.2	17.24 ± 0.11	0.516 ± 0.052
<i>b</i>	1495.0	1687.4	17.52 ± 0.16	0.399 ± 0.059
<i>b</i>	5874.5	6074.3	18.43 ± 0.09	0.172 ± 0.014
<i>b</i>	7310.3	7438.8	18.84 ± 0.30	0.118 ± 0.032
<i>b</i>	99230.7	171611.5	19.80 ± 0.22	0.049 ± 0.010
<i>b</i>	171615.3	172218.5	19.54 ± 0.12	0.062 ± 0.007
<i>u</i>	264.3	514.1	19.43 ± 0.23	0.025 ± 0.005
<i>u</i>	671.6	864.6	18.64 ± 0.34	0.052 ± 0.016
<i>u</i>	1123.8	1317.6	17.27 ± 0.16	0.183 ± 0.027
<i>u</i>	1469.8	1662.5	17.77 ± 0.29	0.115 ± 0.031
<i>u</i>	5669.3	5869.1	18.25 ± 0.11	0.074 ± 0.007
<i>u</i>	7105.2	7304.9	18.56 ± 0.24	0.056 ± 0.012
<i>u</i>	24564.2	24650.4	>18.40	>0.065
<i>u</i>	98317.4	109397.7	19.35 ± 0.18	0.027 ± 0.004
<i>u</i>	264490.8	271341.2	19.89 ± 0.22	0.016 ± 0.003
<i>v</i>	597.5	617.3	>17.72	>0.297
<i>v</i>	771.3	791.0	17.22 ± 0.27	0.471 ± 0.117
<i>v</i>	1050.3	1242.8	16.02 ± 0.10	1.421 ± 0.131
<i>v</i>	1396.2	1589.4	15.81 ± 0.10	1.724 ± 0.159
<i>v</i>	5054.5	5254.2	17.01 ± 0.08	0.571 ± 0.042
<i>v</i>	6490.7	6690.4	17.36 ± 0.10	0.414 ± 0.038
<i>v</i>	17608.5	18515.3	18.49 ± 0.11	0.146 ± 0.015
<i>v</i>	45033.9	45941.0	18.59 ± 0.11	0.133 ± 0.013
<i>v</i>	167595.5	179056.0	18.82 ± 0.12	0.108 ± 0.012
<i>uvw1</i>	647.4	1119.1	18.48 ± 0.36	0.040 ± 0.013
<i>uvw1</i>	1273.5	1638.2	>18.15	>0.054
<i>uvw1</i>	5464.5	5664.2	19.26 ± 0.32	0.019 ± 0.006
<i>uvw1</i>	6900.5	7100.3	18.99 ± 0.32	0.025 ± 0.007
<i>uvw1</i>	23658.1	24557.8	19.74 ± 0.26	0.012 ± 0.003
<i>uvw1</i>	87378.3	104975.0	>20.48	>0.006
<i>uvw1</i>	259190.3	270886.2	20.38 ± 0.33	0.007 ± 0.002
<i>uvw2</i>	4849.7	5049.5	19.19 ± 0.28	0.016 ± 0.004
<i>uvw2</i>	6285.7	6485.5	19.11 ± 0.28	0.017 ± 0.004
<i>uvw2</i>	11637.3	12112.8	20.01 ± 0.33	0.007 ± 0.002
<i>uvw2</i>	27922.6	30389.2	19.71 ± 0.29	0.010 ± 0.003
<i>uvw2</i>	33673.8	40012.9	20.14 ± 0.26	0.007 ± 0.002
<i>uvw2</i>	166688.4	173821.9	>20.62	>0.004
<i>uvm2</i>	5259.3	5459.1	>19.33	>0.014
<i>uvm2</i>	6695.5	6895.2	>19.22	>0.016
<i>uvm2</i>	18520.3	18914.0	>19.63	>0.011
<i>uvm2</i>	22751.2	23651.0	20.39 ± 0.36	0.005 ± 0.002
<i>uvm2</i>	86471.6	103671.5	20.00 ± 0.19	0.008 ± 0.001
<i>uvm2</i>	179061.3	259183.4	20.17 ± 0.29	0.007 ± 0.002
<i>uvm2</i>	269079.1	269978.9	20.38 ± 0.34	0.005 ± 0.002

Note. No correction for Galactic extinction is applied.

ORCID iDs

Vikas Chand  <https://orcid.org/0000-0002-7876-7362>
Ankush Banerjee  <https://orcid.org/0000-0002-4371-2417>
Rahul Gupta  <https://orcid.org/0000-0003-4905-7801>
Dimple  <https://orcid.org/0000-0001-9868-9042>
Partha Sarathi Pal  <https://orcid.org/0000-0001-8922-8391>
Jagdish C. Joshi  <https://orcid.org/0000-0003-3383-1591>
Bin-Bin Zhang  <https://orcid.org/0000-0003-4111-5958>
R. Basak  <https://orcid.org/0000-0001-5488-7258>
P. H. T. Tam  <https://orcid.org/0000-0002-1262-7375>
Vidushi Sharma  <https://orcid.org/0000-0002-4394-4138>
Yi-Si Yang  <https://orcid.org/0000-0002-7555-0790>

References

- Abdalla, H., Adam, R., Aharonian, F., et al. 2019, *Natur*, **575**, 464
Abdo, A. A., Ackermann, M., Ajello, M., et al. 2009, *ApJL*, **706**, L138
Ackermann, M., Ajello, M., Asano, K., et al. 2013, *ApJS*, **209**, 11
Acuner, Z., Ryde, F., Pe'er, A., Mortlock, D., & Ahlgren, B. 2020, *ApJ*, **893**, 128
Ahlgren, B., Larsson, J., Valan, V., et al. 2019, *ApJ*, **880**, 76
Amati, L. 2006, *MNRAS*, **372**, 233
Arnaud, K. A. 1996, in ASP Conf. Ser. 101, Astronomical Data Analysis Software and Systems V, ed. G. H. Jacoby & J. Barnes (San Francisco, CA: ASP), 17
Band, D., Matteson, J., Ford, L., et al. 1993, *ApJ*, **413**, 281
Band, D. L. 1997, *ApJ*, **486**, 928
Barniol Duran, R., & Kumar, P. 2011, *MNRAS*, **412**, 522
Basak, R., & Rao, A. R. 2013, *MNRAS*, **436**, 3082
Basak, R., & Rao, A. R. 2015, *ApJ*, **812**, 156
Bernardini, M. G., Ghirlanda, G., Campana, S., et al. 2015, *MNRAS*, **446**, 1129
Bernardini, M. G., Margutti, R., Chincarini, G., Guidorzi, C., & Mao, J. 2011, *A&A*, **526**, A27
Blazek, M., Izzo, L., Kann, D. A., & de Ugarte Postigo, A. 2019, GCN, **25592**, 1
Bolmer, J., Greiner, J., & Chen, T.-W. 2019, GCN, **25651**, 1
Burgess, J. M., Bégué, D., Greiner, J., et al. 2020, *NatAs*, **4**, 471
Burrows, D. N., Hill, J. E., Nousek, J. A., et al. 2005, *SSRv*, **120**, 165
Chand, V., Pal, P. S., Banerjee, A., et al. 2019, arXiv:1905.11844
Chandra, P. 2019, GCN, **25627**, 1
Chen, T., Bolmer, J., Guelbenzu, A. N., & Klose, S. 2019, GCN, **25569**, 1
Chincarini, G., Mao, J., Margutti, R., et al. 2010, *MNRAS*, **406**, 2113
Curran, P. A., Starling, R. L. C., O'Brien, P. T., et al. 2008, *A&A*, **487**, 533
Dai, Z. G., & Liu, R.-Y. 2012, *ApJ*, **759**, 58
D'Avanzo, P., D'Elia, V., Rossi, A., & Melandri, A. 2019, GCN, **25591**, 1
de Naurois, M. 2019, ATel, **13052**, 1
de Ugarte Postigo, A., Bremer, M., Kann, D. A., & Thoene, C. C. 2019a, GCN, **25589**, 1
de Ugarte Postigo, A., Izzo, L., Thoene, C. C., & Blazek, M. 2019b, GCN, **25677**, 1
Dichiara, S., Bernardini, M. G., Burrows, D. N., & D'Avanzo, P. 2019, GCN, **25552**, 1
Evans, P. A., Beardmore, A. P., Page, K. L., et al. 2007, *A&A*, **469**, 379
Evans, P. A., Beardmore, A. P., Page, K. L., et al. 2009, *MNRAS*, **397**, 1177
Falcone, A. D., Burrows, D. N., Lazzati, D., et al. 2006, *ApJ*, **641**, 1010
Fenimore, E. E., in 't Zand, J. J. M., Norris, J. P., Bonnell, J. T., & Nemiroff, R. J. 1995, *ApJL*, **448**, L101
Fermi GBM Team 2019, GCN, **25551**, 1
Fong, W., Laskar, T., Schroeder, G., & Coppejans, D. 2019, GCN, **25583**, 1
Foreman-Mackey, D., Hogg, D. W., Lang, D., & Goodman, J. 2013, *PASP*, **125**, 306
Frajia, N., de Colle, F., Veres, P., et al. 2017, arXiv:1710.08514
Frajia, N., Dichiara, S., Pedreira, A. C. C. d. E. S., et al. 2019a, *ApJL*, **879**, L26
Frajia, N., Dichiara, S., Pedreira, A. C. C. d. E. S., et al. 2019b, *ApJ*, **885**, 29
Gao, H., Lei, W.-H., Zou, Y.-C., Wu, X.-F., & Zhang, B. 2013, *NewAR*, **57**, 141

- Gibson, S. L., Wynn, G. A., Gompertz, B. P., & O'Brien, P. T. 2017, *MNRAS*, **470**, 4925
- Goldstein, A., Veres, P., Burns, E., et al. 2017, *ApJL*, **848**, L14
- Gottlieb, O., Nakar, E., Piran, T., & Hotokezaka, K. 2018, *MNRAS*, **479**, 588
- Guiriec, S., Connaughton, V., Briggs, M. S., et al. 2011, *ApJL*, **727**, L33
- Guiriec, S., Kouveliotou, C., Daigne, F., et al. 2015a, *ApJ*, **807**, 148
- Guiriec, S., Kouveliotou, C., Hartmann, D. H., et al. 2016, *ApJL*, **831**, L8
- Guiriec, S., Mochkovitch, R., Piran, T., et al. 2015b, *ApJ*, **814**, 10
- Heintz, K., Fynbo, J. P. U., Jakobsson, P., & Xu, D. 2019, GCN, **25563**, 1
- Ioka, K., Kobayashi, S., & Zhang, B. 2005, *ApJ*, **631**, 429
- Kass, R. E., & Rafferty, A. E. 1995, *J. Am. Stat. Assoc.*, **90**, 773
- Kobayashi, S., Zhang, B., Mészáros, P., & Burrows, D. 2007, *ApJ*, **655**, 391
- Kumar, H., Bhalerao, V., Stanzin, J., & Anupama, G. C. 2019, GCN, **25560**, 1
- Kumar, P., & Zhang, B. 2015, *PhR*, **561**, 1
- Lan, L., Lü, H.-J., Zhong, S.-Q., et al. 2018, *ApJ*, **862**, 155
- Laskar, T., Bhandari, S., Schroeder, G., & Fong, W. 2019, GCN, **25676**, 1
- Lazzati, D., & Perna, R. 2007, *MNRAS*, **375**, L46
- Lesage, S., Poolakkil, S., Fletcher, C., & Meegan, C. 2019, GCN, **25575**, 1
- Lien, A., Barthelmy, S. D., Cummings, J. R., & Dichiara, S. 2019, GCN, **25579**, 1
- Lipunov, V., Balakin, F., Gorbvskoy, E., & Kornilov, V. 2019a, GCN, **25558**, 1
- Lipunov, V., Balakin, F., Gorbvskoy, E., & Kornilov, V. 2019b, GCN, **25652**, 1
- MAGIC Collaboration, Acciari, V. A., Ansoldi, S., et al. 2019a, *Natur*, **575**, 455
- MAGIC Collaboration, Acciari, V. A., Ansoldi, S., et al. 2019b, *Natur*, **575**, 459
- Malesani, D., Covino, S., D'Avanzo, P., et al. 2007, *A&A*, **473**, 77
- Matsumoto, T., & Piran, T. 2020, *MNRAS*, **492**, 4283
- Mészáros, P. 2019, *MmSAI*, **90**, 57
- Minaev, P. Y., Pozanenko, A. S., Molkov, S. V., & Grebenev, S. A. 2014, *AstL*, **40**, 235
- Monageng, I., van der Horst, A., Woudt, P., & Bottcher, M. 2019, GCN, **25635**, 1
- Nakar, E., & Sari, R. 2012, *ApJ*, **747**, 88
- Narayana Bhat, P., Meegan, C. A., von Kienlin, A., et al. 2016, *ApJS*, **223**, 28
- Nava, L., Salvaterra, R., Ghirlanda, G., et al. 2012, *MNRAS*, **421**, 1256
- Norris, J. P., Bonnell, J. T., Kazanas, D., et al. 2005, *ApJ*, **627**, 324
- Oates, S., & Dichiara, S. 2019, GCN, **25570**, 1
- Oganesyan, G., Nava, L., Ghirlanda, G., Melandri, A., & Celotti, A. 2019, *A&A*, **628**, A59
- Paek, G. S. H., & Im, M. 2019, GCN, **25584**, 1
- Page, K. L., Starling, R. L. C., Fitzpatrick, G., et al. 2011, *MNRAS*, **416**, 2078
- Panaiteescu, A. 2006, *MNRAS*, **367**, L42
- Perley, D. A., & Cockeram, A. M. 2019a, GCN, **25585**, 1
- Perley, D. A., & Cockeram, A. M. 2019b, GCN, **25597**, 1
- Perley, D. A., & Cockeram, A. M. 2019c, GCN, **25623**, 1
- Perley, D. A., & Cockeram, A. M. 2019d, GCN, **25657**, 1
- Piran, T., & Nakar, E. 2010, *ApJL*, **718**, L63
- Racusin, J. L., Liang, E. W., Burrows, D. N., et al. 2009, *ApJ*, **698**, 43
- Racusin, J. L., Oates, S. R., Schady, P., et al. 2011, *ApJ*, **738**, 138
- Ravasio, M. E., Ghirlanda, G., Nava, L., & Ghisellini, G. 2019a, *A&A*, **625**, A60
- Ravasio, M. E., Oganesyan, G., Ghirlanda, G., et al. 2018, *A&A*, **613**, A16
- Ravasio, M. E., Oganesyan, G., Salafia, O. S., et al. 2019b, *A&A*, **626**, A12
- Ronchi, M., Fumagalli, F., Ravasio, M. E., et al. 2019, arXiv:1909.10531
- Ryde, F. 2005, *ApJL*, **625**, L95
- Scargle, J. D., Norris, J. P., Jackson, B., & Chiang, J. 2013, *ApJ*, **764**, 167
- Schlaflly, E. F., & Finkbeiner, D. P. 2011, *ApJ*, **737**, 103
- Strausbaugh, R., & Cucchiara, A. 2019, GCN, **25641**, 1
- Terreran, G., Fong, W., Margutti, R., & Miller, A. 2019, GCN, **25664**, 1
- Vagnozzi, A., & Nesci, R. 2019, GCN, **25667**, 1
- Valeev, A. F., Castro-Tirado, A. J., Hu, Y. D., & Garcia, E. F. 2019, GCN, **25565**, 1
- Vianello, G., Gill, R., Granot, J., et al. 2017, arXiv:1706.01481
- Volnova, A., Ruyantsev, V., Pozanenko, A., & Belkin, S. 2019, GCN, **25682**, 1
- Wang, X.-G., Zhang, B., Liang, E.-W., et al. 2015, *ApJS*, **219**, 9
- Wang, X.-G., Zhang, B., Liang, E.-W., et al. 2018, *ApJ*, **859**, 160
- Wang, Y., Li, L., Moradi, R., & Ruffini, R. 2019, arXiv:1901.07505
- Xu, D., Yu, B. Y., & Zhu, Z. P. 2019, GCN, **25555**, 1
- Yonetoku, D., Murakami, T., Nakamura, T., et al. 2004, *ApJ*, **609**, 935
- Zhang, B., Liang, E., Page, K. L., et al. 2007, *ApJ*, **655**, 989
- Zhang, B., & Mészáros, P. 2004, *IJMPA*, **19**, 2385
- Zhang, B.-B., Fan, Y.-Z., Shen, R.-F., et al. 2012, *ApJ*, **756**, 190
- Zhang, B. B., Zhang, B., Castro-Tirado, A. J., et al. 2018, *NatAs*, **2**, 69
- Zheng, W., & Filippenko, A. V. 2019, GCN, **25580**, 1